Flow around a rotating, semi-infinite cylinder in an axial stream

S Derebail Muralidhar, B Pier, Julian F. Scott, R Govindarajan

▶ **To cite this version:**

S Derebail Muralidhar, B Pier, Julian F. Scott, R Govindarajan. Flow around a rotating, semi-infinite cylinder in an axial stream. Proceedings of the Royal Society of London. Series A, Mathematical and physical sciences, 2016, 472, pp.20150850. 10.1098/rspa.2015.0850 . hal-01330462

HAL Id: hal-01330462
https://hal.science/hal-01330462

Submitted on 10 Jun 2016

HAL is a multi-disciplinary open access archive for the deposit and dissemination of scientific research documents, whether they are published or not. The documents may come from teaching and research institutions in France or abroad, or from public or private research centers.

L'archive ouverte pluridisciplinaire **HAL**, est destinée au dépôt et à la diffusion de documents scientifiques de niveau recherche, publiés ou non, émanant des établissements d'enseignement et de recherche français ou étrangers, des laboratoires publics ou privés.

PROCEEDINGS A

rspa.royalsocietypublishing.org

Research

Cite this article: Derebail Muralidhar S, Pier B, Scott JF, Govindarajan R. 2016 Flow around a rotating, semi-infinite cylinder in an axial stream. *Proc. R. Soc. A* **472**: 20150850.
http://dx.doi.org/10.1098/rspa.2015.0850

Received: 11 December 2015
Accepted: 9 May 2016
Published: 8 June 2016

Subject Areas:
fluid mechanics, applied mathematics

Keywords:
rotating body, wall jet, boundary layer, asymptotic analysis

Author for correspondence:
Benoît Pier
e-mail: benoit.pier@ec-lyon.fr

THE ROYAL SOCIETY
PUBLISHING

Flow around a rotating, semi-infinite cylinder in an axial stream

S. Derebail Muralidhar[1], B. Pier[1], J. F. Scott[1] and R. Govindarajan[2]

[1] Laboratoire de mécanique des fluides et d'acoustique (École centrale de Lyon–CNRS—Université de Lyon 1–INSA Lyon), 36 avenue Guy-de-Collongue, F-69134 Écully, France.
[2]Centre for Interdisciplinary Sciences, Tata Institute of Fundamental Research, 21 Brundavan Colony, Narsingi, Hyderabad, 500075, India

This paper concerns steady, high-Reynolds-number flow around a semi-infinite, rotating cylinder placed in an axial stream and uses boundary-layer type of equations which apply even when the boundary-layer thickness is comparable to the cylinder radius, as indeed it is at large enough downstream distances. At large rotation rates, it is found that a wall jet appears over a certain range of downstream locations. This jet strengthens with increasing rotation, but first strengthens then weakens as downstream distance increases, eventually disappearing, so the flow recovers a profile qualitatively similar to a classical boundary layer. The asymptotic solution at large streamwise distances is obtained as an expansion in inverse powers of the logarithm of the distance. It is found that the asymptotic radial and axial velocity components are the same as for a non-rotating cylinder, to all orders in this expansion.

1. Introduction

When a semi-infinite rotating cylindrical body is placed in a high-Reynolds-number axial flow (see figure 1), an axisymmetric boundary layer develops along the cylinder. Initially thin, this layer becomes of thickness comparable with, then larger than the cylinder radius at sufficiently large axial distances. Our original motivation for studying this flow was to undertake a stability analysis. However, it soon became clear that there are very few existing studies of the underlying flow,

© The Author(s) Published by the Royal Society. All rights reserved.

despite its interesting features, e.g. the appearance of an axial wall jet beyond a certain threshold value of the rotation rate. The presence of curvature and rotation means that the classical Prandtl equations need to be generalized to allow for these effects. In particular, rotation leads to a centrifugal term which couples all three velocity components. This results in significant qualitative changes in the flow structure, e.g. the wall jet, compared with Blasius flow on a flat plate.

The non-rotating version of this problem was studied analytically by Seban & Boyd [1] using a series solution in powers of $z^{1/2}$, where z is the axial coordinate, non-dimensionalized using the cylinder radius. This series solution was limited to order 3, and thus only applicable close to the inlet. Kelly [2] showed that the series solution for the displacement thickness provided by Seban & Boyd [1] was erroneous, and obtained the correct result. Glauert & Lighthill [3] extended this work to obtain a solution at all z using the Pohlhausen approximation . At large z, Glauert & Lighthill [3] also showed that the velocity profile had an asymptotic expansion in inverse powers of $\log(z)$. Jaffe & Okamura [4] were the first to solve the boundary-layer equations for this problem numerically, thus covering the entire range of z, from small to large values. Boundary-layer velocity profiles have also been numerically determined by Tutty *et al.* [5] and Vindod & Govindarajan [6] in the context of stability analysis.

Petrov [7] appears to be the first to have studied the rotating case. Axial velocity profiles were obtained in the limit of small z and show the existence of a wall jet for sufficiently strong rotation, though this interesting feature was not explained in the paper. Motivated as we were by stability analysis of the flow, Kao & Chow [8] and Herrada *et al.* [9] solved the present problem numerically. However, both papers limit themselves to a range of rotation rates insufficiently large to produce a wall jet. Furthermore, the centrifugal term is missing in the boundary-layer equations of Kao & Chow [8], and so they are incapable of yielding a wall jet even at large rotation rates.

In §2, we define the two non-dimensional control parameters of the problem, Re and S, the Reynolds number and non-dimensional rotation rate. The boundary-layer equations, valid for large Re, and allowing for boundary-layer thickness to be comparable with the cylinder radius are given. These equations generalise the Prandtl equations and apply for arbitrary (not necessarily small) ratios of boundary-layer thickness to cylinder radius. Suitable rescaling of the variables renders the problem independent of Re, leaving only S as control parameter. Section 3 describes the numerical scheme and its verification, while §4 gives results and discussion, in particular focussing on the wall jet. Finally, §5 gives asymptotic analyses of the limits of large $Z = z/\mathrm{Re}$ and large S. The boundary layer on the nose is discussed in the appendices. It is found that the precise shape of the nose is unimportant: the input to the boundary-layer equations of §2 being the Blasius flat-plate flow (generalized to include the azimuthal component due to rotation), independent of the nose shape.

2. Boundary-layer equations

A semi-infinite cylinder of radius a rotates about its axis with angular velocity Ω and is placed in an axial stream of incompressible fluid of velocity U_∞ and viscosity ν (see figure 1). Assuming large Reynolds number, an initially thin boundary layer develops along the cylinder. If the cylinder were sharply truncated at the nose, flow separation would occur as is usually the case at a salient edge [10]. To avoid this scenario we assume there is a smooth nose, as shown in figure 1. Another way to avoid flow separation would be to consider a thin hollow cylinder. The boundary-layer equations formulated in this section hold good for both these cases. A detailed analysis of the nose region is given in appendix B.

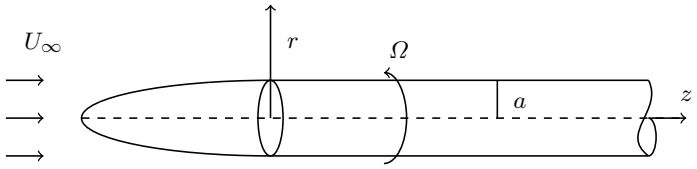

Figure 1. Schematic diagram of the problem.

The natural length and velocity scales are a and U_∞. These scales are used to non-dimensionalize the axisymmetric, steady Navier–Stokes equations in cylindrical coordinates, z, r, θ. There are two non-dimensional parameters, namely the Reynolds number

$$\mathrm{Re} = \frac{U_\infty a}{\nu}, \tag{2.1}$$

and the rotation rate

$$S = \frac{\Omega a}{U_\infty}. \tag{2.2}$$

Assuming a large Reynolds number, the length scale for axial variation of the flow is much longer than that for radial variation. This separation of scales leads to the boundary-layer approximation. Thus,

$$u_z \frac{\partial u_z}{\partial z} + u_r \frac{\partial u_z}{\partial r} = -\frac{\partial p}{\partial z} + \frac{1}{\mathrm{Re}} \left(\frac{\partial^2 u_z}{\partial r^2} + \frac{1}{r} \frac{\partial u_z}{\partial r} \right), \tag{2.3}$$

$$\frac{u_\theta^2}{r} = \frac{\partial p}{\partial r}, \tag{2.4}$$

$$u_z \frac{\partial u_\theta}{\partial z} + u_r \frac{\partial u_\theta}{\partial r} + \frac{u_\theta u_r}{r} = \frac{1}{\mathrm{Re}} \left(\frac{\partial^2 u_\theta}{\partial r^2} + \frac{1}{r} \frac{\partial u_\theta}{\partial r} - \frac{u_\theta}{r^2} \right), \tag{2.5}$$

$$\frac{\partial u_z}{\partial z} + \frac{1}{r} \frac{\partial r u_r}{\partial r} = 0 \tag{2.6}$$

are obtained by dropping terms of higher order from the Navier–Stokes equations in the usual manner. Note that we have not assumed the boundary layer to be thin compared with the radius. The boundary conditions are

$$u_z = 0, u_r = 0, u_\theta = S \quad z > 0, r = 1, \tag{2.7}$$

$$u_z \to 1, u_\theta \to 0, p \to 0 \quad z > 0, r \to \infty. \tag{2.8}$$

The above equations contain the azimuthal component, u_θ, of the velocity. This is due to rotation of the cylinder, which induces the centrifugal term on the left-hand side of equation (2.4), leading to a significant radial pressure gradient. Such an effect is not present in classical boundary-layer theory, which predicts near constancy of the pressure across the layer. Compared to the Prandtl equations of a classical boundary layer, equations (2.3)–(2.6) allow for the additional effects of both rotation and curvature. Near the nose the boundary layer is thin compared with the cylinder radius and curvature effects are negligible. But at large z, boundary-thickening eventually makes the thickness comparable to, then larger compared with the radius, and the full set of equations is required.

The above problem needs to be completed by inlet conditions. At distances from the nose of $O(a)$, the boundary layer is thin compared to the radius and is described by the axisymmetric Prandtl equations given in appendix B. On the cylinder (after leaving the nose), these equations

become the flat-plate Prandtl equations, and as z increases, we expect the flow to forget the precise initial conditions and to approach the Blasius solution, independent of the nose shape (here, we implicitly suppose the nose length to be of the same order as its diameter). There are, in fact, two asymptotic regions, $z = O(1)$, where the equations of appendix B apply, and $z = O(Re)$, where the boundary-layer thickness is comparable to the cylinder radius and equations (2.3)–(2.8) hold. Matching between these regions requires that the inlet condition be the Blasius solution (generalized to include the azimuthal component due to rotation). The same is true for the case of the hollow cylinder. In either case, equations (2.3)–(2.8) are supplemented by Blasius initial conditions as $z \to 0$.

Introducing the scaled variables

$$R = r, \quad Z = \frac{z}{\mathrm{Re}}, \tag{2.9}$$

$$U_z = u_z, \quad U_r = R u_r \mathrm{Re}, \quad U_\theta = R u_\theta, \quad P = R^2 p, \tag{2.10}$$

equations (2.3)–(2.8) become

$$U_z \frac{\partial U_z}{\partial Z} + \frac{U_r}{R}\frac{\partial U_z}{\partial R} = -\frac{1}{R^2}\frac{\partial P}{\partial Z} + \frac{\partial^2 U_z}{\partial R^2} + \frac{1}{R}\frac{\partial U_z}{\partial R}, \tag{2.11}$$

$$U_\theta^2 = R\frac{\partial P}{\partial R} - 2P, \tag{2.12}$$

$$U_z \frac{\partial U_\theta}{\partial Z} + \frac{U_r}{R}\frac{\partial U_\theta}{\partial R} = \frac{\partial^2 U_\theta}{\partial R^2} - \frac{1}{R}\frac{\partial U_\theta}{\partial R}, \tag{2.13}$$

$$\frac{\partial U_z}{\partial Z} + \frac{1}{R}\frac{\partial U_r}{\partial R} = 0, \tag{2.14}$$

$$U_z = U_r = 0, U_\theta = S \qquad R = 1, \tag{2.15}$$

$$U_z \to 1, U_\theta = 0, P = 0 \qquad R \to \infty. \tag{2.16}$$

It is apparent that, using these scalings, Re has disappeared from the problem, leaving S as the only non-dimensional parameter. This result indicates, among other things, that the natural scaling of the axial coordinate is $z = O(\mathrm{Re})$. Thus, as noted earlier, the distance needed for the boundary-layer thickness to become comparable with the radius is Re times the radius. The factors of R appearing in equation (2.10) have been introduced to improve numerical convergence.

3. Numerical scheme and validation

The boundary-layer thickness goes to zero like $Z^{1/2}$ and $U_r \to \infty$ like $Z^{-1/2}$ as $Z = 0$ is approached. To maintain numerical accuracy in the presence of such singular behaviour, we introduce the variables

$$\zeta = (2Z)^{\frac{1}{2}}, \quad \sigma = \frac{R-1}{\zeta}, \quad V_r = \zeta U_r, \quad V_z = U_z, \quad V_\theta = U_\theta. \tag{3.1}$$

Here, the boundary-layer thickness is prevented from going to zero in the radial coordinate σ by dividing $R - 1$ by ζ. V_r is kept finite by use of the factor ζ and ζ is used in place of Z to make the solution a smooth function of the axial coordinate. Using these variables in the boundary-layer

equations (2.11)–(2.16) results in

$$\zeta V_z \frac{\partial V_z}{\partial \zeta} + \left(\frac{V_r - \zeta}{R} - \sigma V_z \right) \frac{\partial V_z}{\partial \sigma} = \frac{1}{R^2} (\sigma \frac{\partial P}{\partial \sigma} - \zeta \frac{\partial P}{\partial \zeta}) + \frac{\partial^2 V_z}{\partial \sigma^2}, \tag{3.2}$$

$$\frac{\zeta}{R} \left(V_\theta^2 + 2P \right) = \frac{\partial P}{\partial \sigma}, \tag{3.3}$$

$$\zeta V_z \frac{\partial V_\theta}{\partial \zeta} + \left(\frac{V_r + \zeta}{R} - \sigma V_z \right) \frac{\partial V_\theta}{\partial \sigma} = \frac{\partial^2 V_\theta}{\partial \sigma^2}, \tag{3.4}$$

$$\zeta \frac{\partial V_z}{\partial \zeta} - \sigma \frac{\partial V_z}{\partial \sigma} + \frac{1}{R} \frac{\partial V_r}{\partial \sigma} = 0, \tag{3.5}$$

with the boundary conditions

$$V_z = V_r = 0, V_\theta = S \qquad \sigma = 0, \tag{3.6}$$

$$V_z \to 1, V_\theta = 0, P = 0 \qquad \sigma \to \infty. \tag{3.7}$$

These equations govern the axial evolution of the flow. The inlet condition (Blasius solution) is obtained by setting $\zeta = 0$ and solving the resulting equations.

The radial coordinate σ is discretized using Chebyshev collocation points:

$$x_n = \cos \left(\frac{n\pi}{N-1} \right) \qquad 0 \le n < N, \tag{3.8}$$

$$\sigma_n = \frac{\hat{\sigma}(1 + x_n)}{1 - x_n}, \qquad x \in [-1, 1] \to \sigma \in [0, \infty]. \tag{3.9}$$

The parameter $\hat{\sigma}$ controls the distribution of points such that half of them lie between $0 \le \sigma \le \hat{\sigma}$. The velocities V_z and V_θ are represented by their values at all collocation points. However, since there is no boundary condition for the pressure at the surface, it is represented at all points except $\sigma = 0$. Similarly, there is no boundary condition for V_r at $\sigma = \infty$ and so it is represented at all points apart from $\sigma = \infty$. The Chebyshev derivative matrices for P and V_r are correspondingly modified (e.g. appendix A in [12]).

The coordinate ζ is discretised using small, equally-spaced steps, $\zeta_i = i\Delta$, and the variables V_z, V_r, V_θ, P are represented by their values at ζ_i. Equations (3.2), (3.4) and (3.5) are evaluated at mid-step, $\zeta_{i+\frac{1}{2}}$, using an implicit scheme that employs centered finite differencing to represent the ζ-derivatives. Equation (3.3) is evaluated at the step position ζ_i, rather than at the midstep. At each step, the equations are solved using Newton–Raphson iteration, thus allowing forward marching. The inlet solution is obtained from equations (3.2)–(3.7) using $\zeta = 0$. Following discretization in σ using the collocation points, the result is again obtained by Newton–Raphson iteration.

The code was first tested by changing the numerical parameters $N, \hat{\sigma}, \Delta$, and observing the dependence of the solution on these parameters. Based on the convergence results we decided to use $N = 128, \hat{\sigma} = 5, \Delta = 0.001$ in our computations. These values gave convergence to better than seven decimal places. The code was also tested using the volume-flux and momentum balance equations. The results respect these equations to seven decimal places. Although use of the Blasius solution at the inlet has earlier been justified by an asymptotic argument, it is interesting to see the effect of a change in inlet profile on the solution. Thus we modified the inlet profile to be $U_z^* = U_z + A\sigma \exp(-0.5\sigma)$, where U_z is the Blasius profile. Taking $A = 2$, it was found that the change in the U_z at $Z = 2$ was in the sixth decimal place. This illustrates the fact that the flow forgets the initial condition as Z increases and becomes insensitive to the precise inlet profile used.

We also validated the code by comparing our results with the existing literature. Tutty *et al.* [5] studied the case without rotation. The axial (x_t) and radial (σ_t) coordinates used by Tutty *et al.* [5]

are related to those used here via $x_t/\mathrm{Re} = Z$ and $\sigma_t = \sqrt{2}\sigma$. Figure 2 shows good agreement with our results for $\mathrm{Re} = 10^4$, $x_t = 0.01$ and $x_t = 10^5$. Herrada *et al.* [9] considered the problem of the rotating cylinder. They do not give velocity profiles, but rather the skin friction on the cylinder:

$$\tau = \left.\frac{\partial U_z(Z)}{\partial R}\right|_{R=1} = \left.\frac{1}{\zeta}\frac{\partial V_z(\zeta)}{\partial \sigma}\right|_{\sigma=0}. \tag{3.10}$$

Figure 2 shows τ as a function of Z for $S = 1$ and good agreement is apparent.

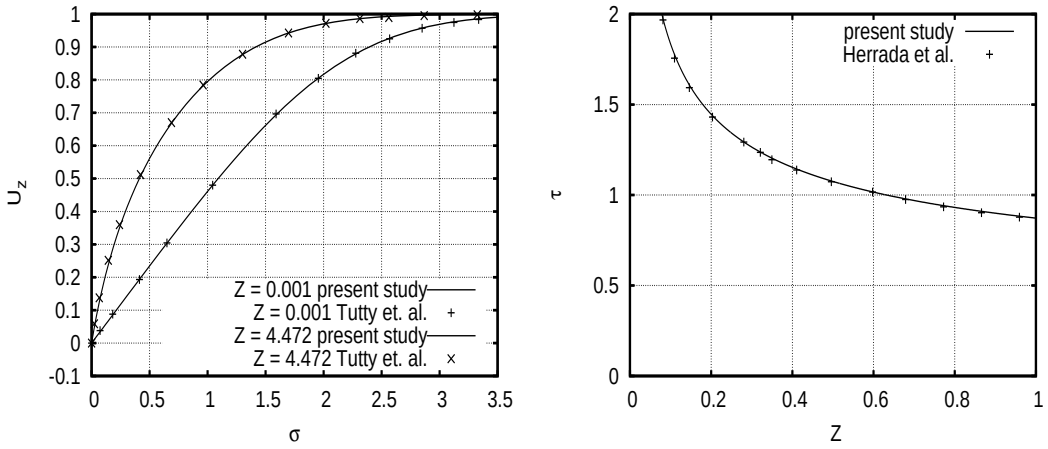

Figure 2. Comparison of U_z for $S = 0$ at two values of Z with [5] and comparison of skin friction τ for $S = 1$ with [9].

4. Results

Flow profiles were obtained for different values of S and Z. Figure 3 shows velocity profiles for $S = 0.1$ and different values of Z. For $Z = 0$, $V_z(\sigma)$ corresponds to the Blasius flat-plate solution. As Z increases, $V_z(\sigma)$ deviates from the Blasius profile due to cylinder curvature and rotation. It should be borne in mind that the boundary-layer thickness increases with Z, although this is not apparent in the figure because the scaled radial coordinate $\sigma = (R-1)/\zeta$ has been used. Note that the azimuthal velocity at $Z = 0$ is $V_\theta(\sigma) = S\big(1 - V_z(\sigma)\big)$. As Z increases, small departures from this profile arise. Figure 4 and figure 5 show results for $Z = 0.5$ and different values of S. When $S \lesssim 1$, $V_z(\sigma)$ is a modified Blasius profile. However, for $S \gtrsim 4$, $V_z(\sigma)$ is no longer monotonic having a maximum at finite σ. At large S, the maximum is large and the profile is better described as an axial wall jet, rather than a boundary layer. At first sight, it is perhaps surprising that increasing the rotation rate leads to a stronger and stronger axial flow. Increasing S causes V_θ to increase (see figure 4). This in turn produces an increasing radial pressure gradient due to the centrifugal force. Since the pressure is constant outside the boundary layer, the pressure within the layer drops (see figure 5) with Z. The development of the flow means that the axial presure gradient becomes larger and larger, thus driving a strong axial wall jet. Whereas for lower values of S, boundary-layer thickening leads to positive V_r, at large S entrainment by the wall jet gives negative V_r outside the layer (see figure 4).

The existence of a wall jet at large S is apparent in the axial velocity profiles given by Petrov [7]. However, that article only gives such profiles for the case of small Z (thin boundary layer) and no explanation is provided. Petrov [7] also gives the maximum axial velocity $U_z^{\max} = \max_R(U_z(R))$ as a function of Z. Figure 6 shows a comparison with our results. A small difference is apparent,

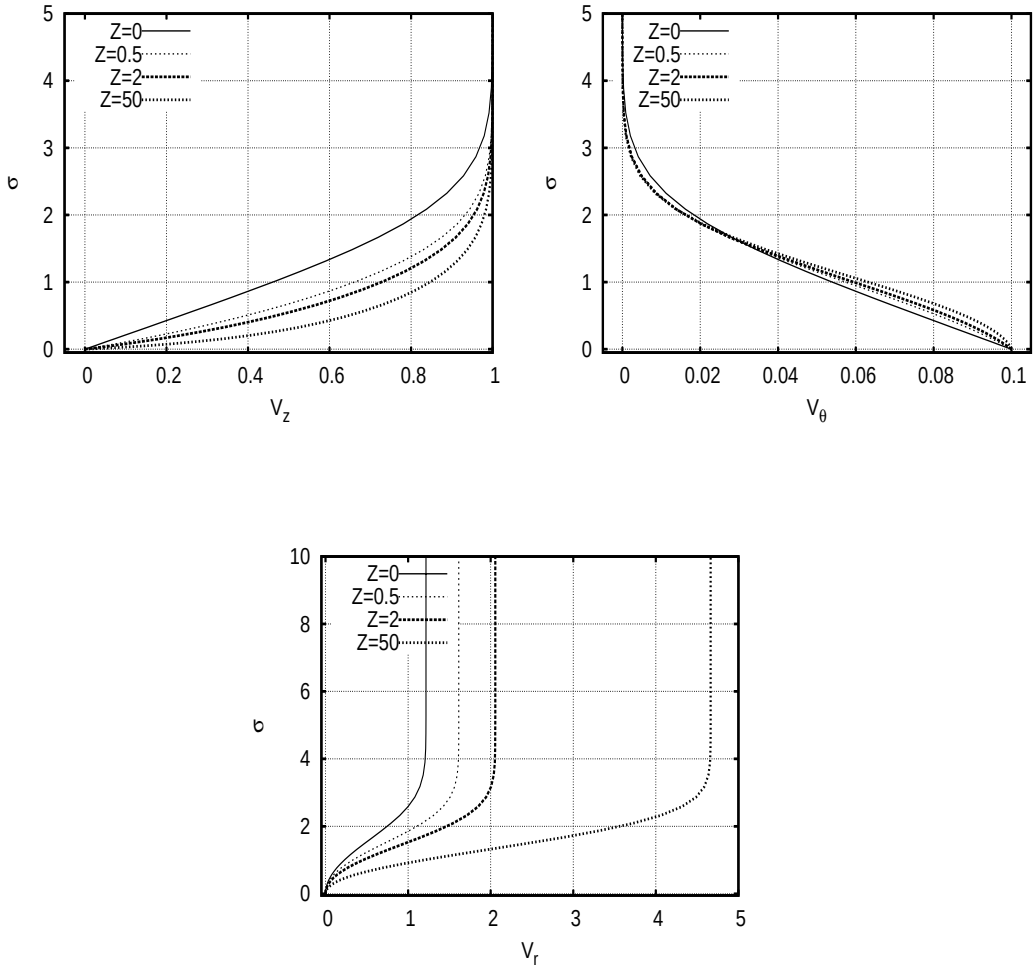

Figure 3. Velocity profiles $V_z(\sigma)$, $V_\theta(\sigma)$ and $V_r(\sigma)$ for different axial positions Z at $S = 0.1$.

the origin of which is unclear.

Figure 7 shows contours of constant $U_z^{\max}$ in the (S, ζ)-plane as well as the boundary (solid line) separating the region in which $U_z^{\max} = 1$ from that in which $U_z^{\max} > 1$ (which we interpret as indicating a wall jet). It will be seen that there is a threshold, $S = 4.15$, below which $U_z^{\max} = 1$. Above this value, the wall jet exists for some range of axial position. Note that, whatever the strength of rotation, the wall jet eventually disappears sufficiently far downstream.

The thickness of the boundary layer/wall jet can be measured using

$$\delta = \frac{1}{U_z^{\max}} \int_1^\infty |1 - U_z| \mathrm{d}R. \tag{4.1}$$

The absolute value is taken to make the integral always positive and the division by $U_z^{\max}$ allows for the strong wall jets which arise at large S. Figure 8 shows $\delta(Z)$ for different values of S. The layer thickness is seen to increase with Z in a roughly parabolic manner (recall that the thickness behaves as $Z^{\frac{1}{2}}$ for small Z). Thickening of the layer is due to viscous diffusion in

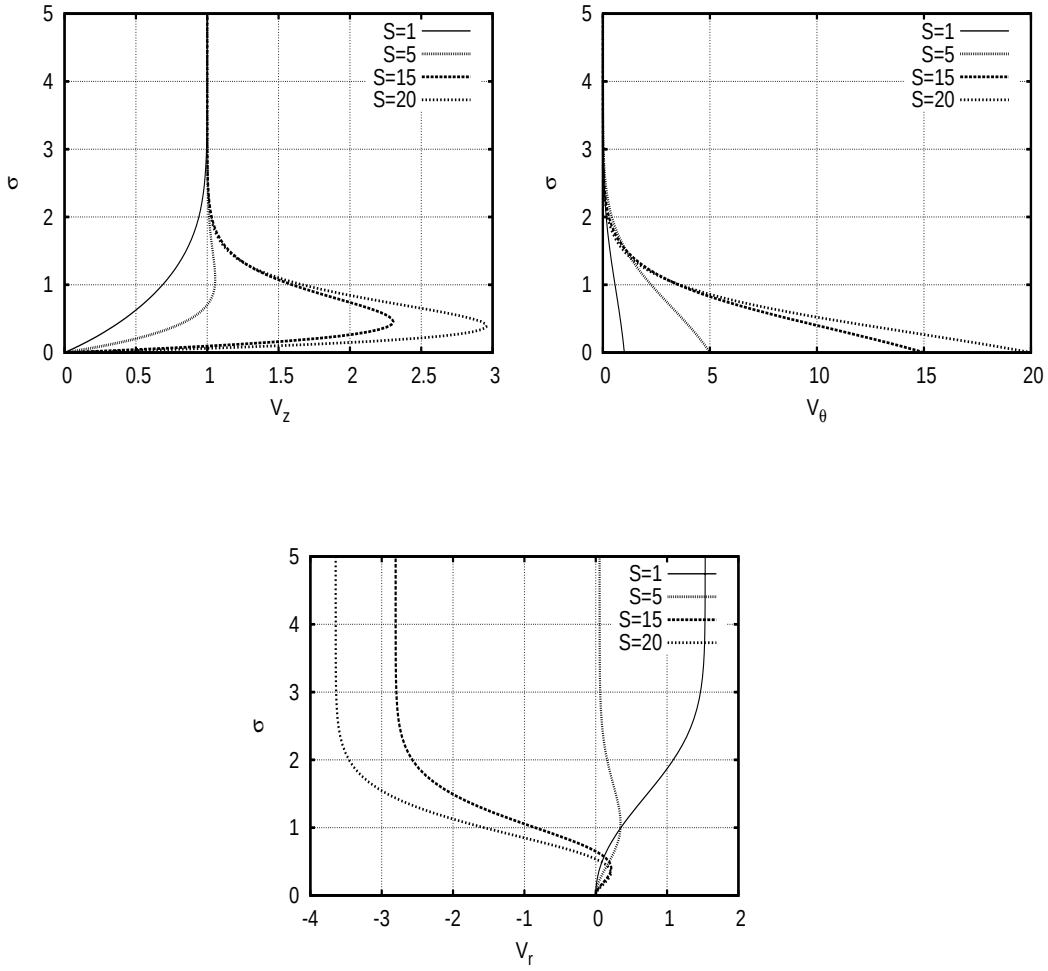

Figure 4. Velocity profiles $V_z(\sigma)$, $V_\theta(\sigma)$ and $V_r(\sigma)$ at $Z = 0.5$ for different values of rotation rate S.

the usual manner. Increasing S causes the layer to become thinner. At large S, the wall jet is of increasing strength. Viscous diffusion competes with axial convection, the latter being of growing importance, hence the decrease of δ with increasing S.

5. Asymptotic analysis

(a) Large-Z asymptotics

Suitable coordinates are

$$\eta = R/\zeta, \quad \chi = \ln(\zeta). \tag{5.1}$$

Here, we have followed Glauert & Lighthill [3], who used a logarithmic axial coordinate for the non-rotating cylinder problem. This coordinate reflects slower and slower evolution of the flow in

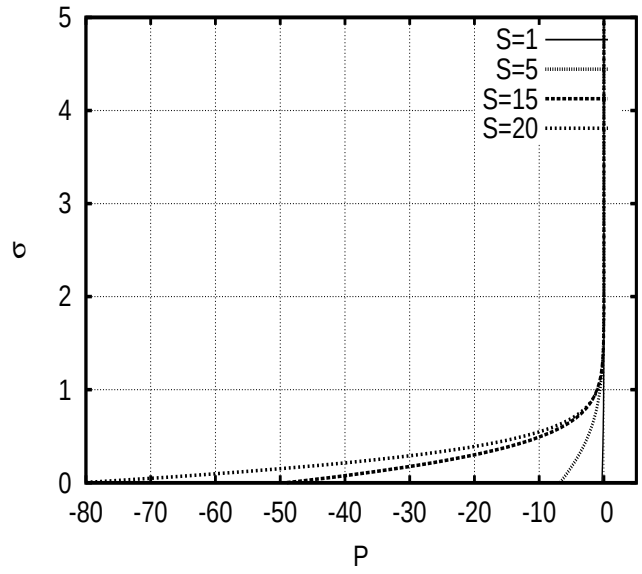

Figure 5. Pressure profile $P(\sigma)$ at $Z = 0.5$ for different values of S.

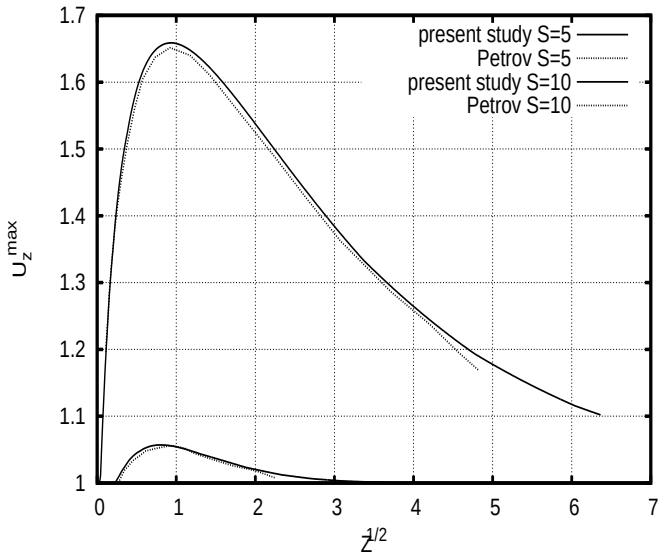

Figure 6. Comparison of $U_z^{\max}$ as a function of $Z^{1/2}$ obtained by the present study with [7] for the case of $S = 5$ and $S = 10$.

the streamwise direction as Z increases. Using these coordinates, equations (2.11)–(2.16) become

$$U_z\left(\frac{\partial U_z}{\partial \chi} - \eta\frac{\partial U_z}{\partial \eta}\right) + \frac{U_r}{\eta}\frac{\partial U_z}{\partial \eta} = \frac{\mathrm{e}^{-2\chi}}{\eta^2}\left(\eta\frac{\partial P}{\partial \eta} - \frac{\partial P}{\partial \chi}\right) + \frac{\partial^2 U_z}{\partial \eta^2} + \frac{1}{\eta}\frac{\partial U_z}{\partial \eta}, \tag{5.2}$$

$$U_\theta^2 + 2P = \eta\frac{\partial P}{\partial \eta}, \tag{5.3}$$

$$U_z\left(\frac{\partial U_\theta}{\partial \chi} - \eta\frac{\partial U_\theta}{\partial \eta}\right) + \frac{U_r}{\eta}\frac{\partial U_\theta}{\partial \eta} = \frac{\partial^2 U_\theta}{\partial \eta^2} - \frac{1}{\eta}\frac{\partial U_\theta}{\partial \eta}, \tag{5.4}$$

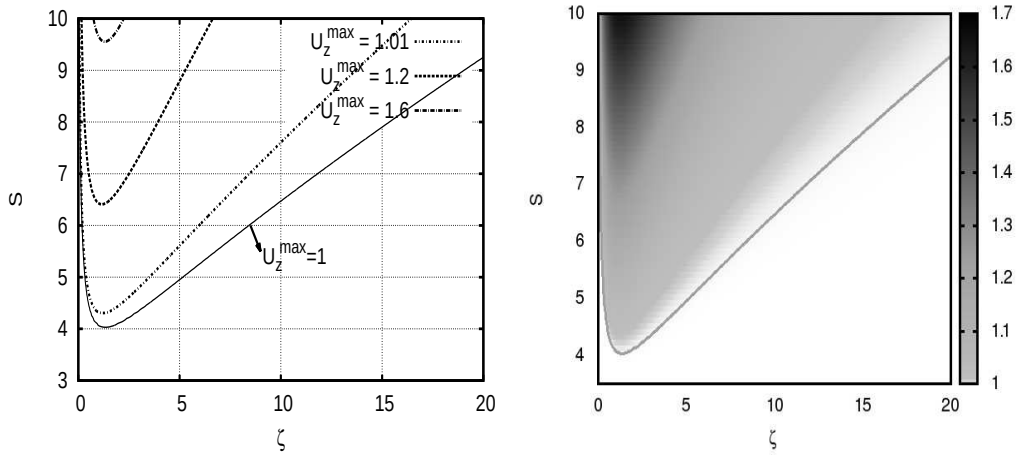

Figure 7. Grayscale plot of $U_z^{\max}$ alongside a contour plot of $U_z^{\max}$. The figure also shows the boundary (solid line) between $U_z^{\max} = 1$ and $U_z^{\max} > 1$.

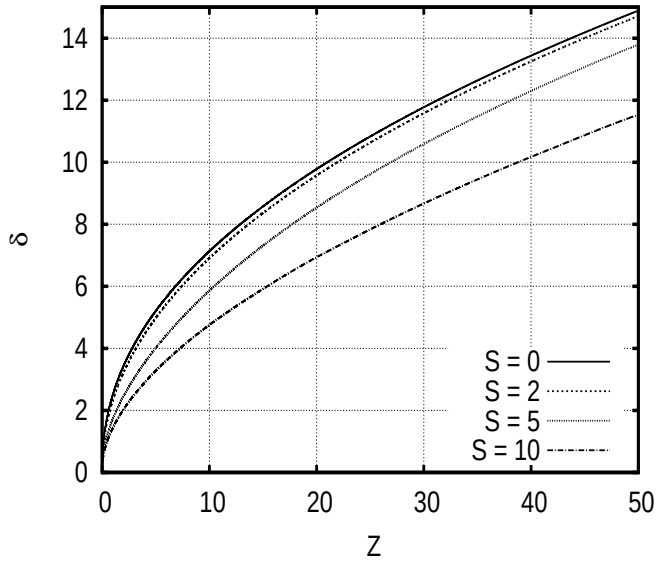

Figure 8. Boundary-layer/wall-jet thickness δ versus Z for different values of S.

$$\frac{\partial U_z}{\partial \chi} - \eta \frac{\partial U_z}{\partial \eta} + \frac{1}{\eta}\frac{\partial U_r}{\partial \eta} = 0, \tag{5.5}$$

$$U_z = U_r = 0, U_\theta = S \quad \eta = e^{-\chi}, \tag{5.6}$$

$$U_z \to 1, U_\theta \to 0, P \to 0 \quad \eta \to \infty. \tag{5.7}$$

It is shown in appendix A that U_z, U_r, U_θ and P have asymptotic expansions in powers of χ^{-1}. The factor of $\mathrm{e}^{-2\chi}$ in equation (5.2) is exponentially small and is hence negligible at all algebraic orders. Without the corresponding term in equation (5.2), U_z and U_r decouple from U_θ and P, though the latter depends on the former. Thus, we expect such decoupling to hold at all orders.

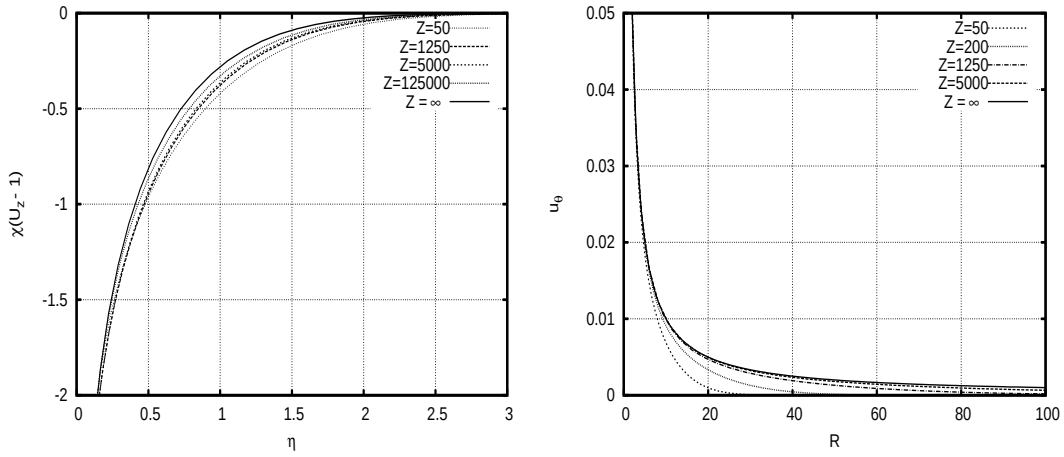

Figure 9. Comparison of $\chi(U_z - 1)$ and $u_\theta = U_\theta/R$ for different values of Z at $S = 0.1$ with the $Z \to \infty$ solution.

This is indeed what is found in appendix A, where the governing equations for the coefficients of the expansions in powers of χ^{-1} are obtained for all orders. Given decoupling, rotation does not enter into the asymptotics of U_z and U_r, which are consequently the same as for the non-rotating case.

Glauert & Lighthill [3] studied the case without rotation and obtained the expansions of U_z and U_r. Appendix A extends the analysis to include rotation and gives detailed results up to order 5. At first order, the asymptotic solution can be obtained analytically and is given by

$$U_z \sim 1 - \chi^{-1} \int_\eta^\infty \frac{\mathrm{e}^{-\xi^2/2}}{\xi} \mathrm{d}\xi, \tag{5.8}$$

$$U_r \sim \chi^{-1}(1 - \mathrm{e}^{-\eta^2/2}), \tag{5.9}$$

$$U_\theta \sim S\mathrm{e}^{-\eta^2/2}, \tag{5.10}$$

$$P \sim -S^2\eta^2 \int_\eta^\infty \frac{\mathrm{e}^{-\xi^2}}{\xi^3} \mathrm{d}\xi. \tag{5.11}$$

In figure 9, the results for U_z show convergence to the asymptotic form (5.8), while those for $u_\theta = U_\theta/R$ converge to $u_\theta \sim S/R$, which is the flow due to a rotating cylinder, infinite in both axial directions (rather than semi-infinite) and without axial flow.

(b) Large-S asymptotics

As we saw in the previous section, the numerical results show the existence of a wall jet at large S. In this limit, appropriate scaled variables are

$$Z^* = \frac{Z}{S}, \quad R^* = R, \tag{5.12}$$

$$U_z^* = \frac{U_z}{S}, \quad U_r^* = U_r, \quad U_\theta^* = \frac{U_\theta}{S}, \quad P^* = \frac{P}{S^2}. \tag{5.13}$$

The scaling of Z reflects the increasing distance required for flow development as the rotation rate increases. The scaling of U_z and U_θ indicates the strengthening flow velocity as S increases. The large-S asymptotic expansions of U_z^*, U_r^*, U_θ^* and P^* proceed as powers of S^{-1}. At leading

order (S^0), we find

$$U_z^* \frac{\partial U_z^*}{\partial Z^*} + \frac{U_r^*}{R^*}\frac{\partial U_z^*}{\partial R^*} = -\frac{1}{R^{*2}}\frac{\partial P^*}{\partial Z^*} + \frac{\partial^2 U_z^*}{\partial R^{*2}} + \frac{1}{R^*}\frac{\partial U_z^*}{\partial R^*}, \tag{5.14}$$

$$U_\theta^{*2} = R^* \frac{\partial P^*}{\partial R^*} - 2P^*, \tag{5.15}$$

$$U_z^* \frac{\partial U_\theta^*}{\partial Z^*} + \frac{U_r^*}{R^*}\frac{\partial U_\theta^*}{\partial R^*} = \frac{\partial^2 U_\theta^*}{\partial R^{*2}} - \frac{1}{R^*}\frac{\partial U_\theta^*}{\partial R^*}, \tag{5.16}$$

$$\frac{\partial U_z^*}{\partial Z^*} + \frac{1}{R^*}\frac{\partial U_r^*}{\partial R^*} = 0, \tag{5.17}$$

with the following inlet and boundary conditions

$$U_z^* = 0, U_\theta^* = 0 \quad Z^* = 0, \tag{5.18}$$

$$U_z^* = 0, U_r^* = 0, U_\theta^* = 1 \quad R^* = 1, \tag{5.19}$$

$$U_z^* = 0, U_\theta^* = 0, P^* = 0 \quad R^* \to \infty. \tag{5.20}$$

Figure 10 shows the solution of the above problem (solid line) compared with the numerical results discussed before for $Z^* = 0.1$ and different values of S. It is apparent that the asymptotics are indeed approached as $S \to \infty$. Figure 11 shows the leading-order asymptotic solution for different values of Z^*. We see that the large-Z limit ($u_\theta \sim SR^{-1}$) is approached by u_θ as $Z^* \to \infty$.

Note that the limit $S \to \infty$ can be reached in two ways: either by increasing the rotation rate, or by decreasing the velocity U_∞ to zero. Note also that u_z/S and u_θ/S are the velocity components non-dimensionalized by Ωa, rather than U_∞, and that $Z^* = z/\mathrm{Re}_\Omega$, where $\mathrm{Re}_\Omega = \Omega a^2/\nu$ is the Reynolds number based on the rotational velocity Ωa. Thus figure 11 can be interpreted as showing the flow due to a rotating, semi-infinite cylinder in a still fluid ($U_\infty = 0$). It can be shown that the separation of radial and axial length scales, which underlies the boundary-layer type approximation we have used, is valid if either of the Reynolds numbers, Re or Re_Ω, is large.

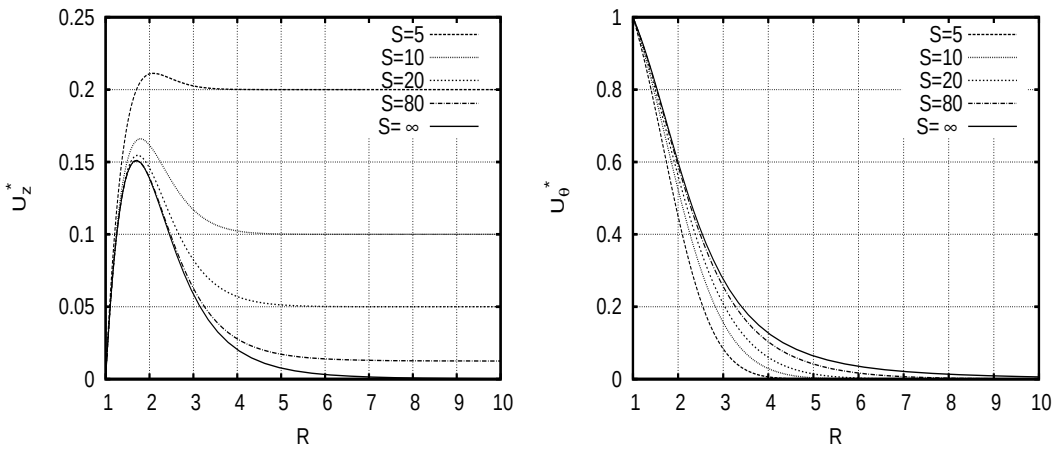

Figure 10. Comparison of U_z^* and U_θ^* for different values of S and $Z^* = 0.1$ with the $S \to \infty$ asymptotic solution.

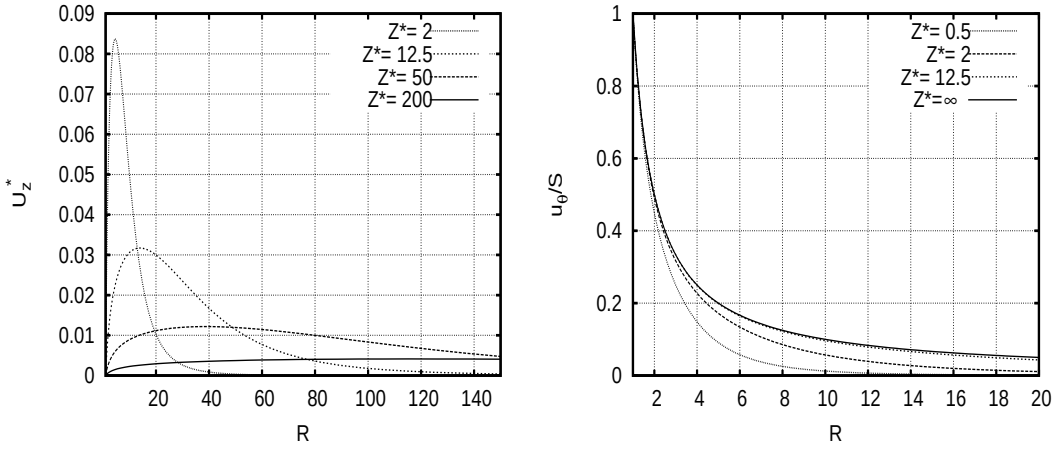

Figure 11. $u_z/S = U_z^*$ and u_θ/S at different values of Z^* for a rotating cylinder in the limit $S \to \infty$.

6. Conclusion

In this paper we have presented a study of the flow around a rotating cylinder in an axial stream. We have assumed a smooth nose to avoid flow separation. The two non-dimensional control parameters of the problem are: Reynolds number (Re) and rotation rate (S). The flow equations are formulated using a boundary-layer type approximation, appropriate at large Reynolds numbers and in which the flow is assumed to evolve slowly in the streamwise direction in comparison to the radial direction. The resulting equations are not limited to the case in which the boundary layer is thin compared with the cylinder radius. By using appropriate scalings we remove Re from the problem.

The results show that the boundary-layer thickness increases with axial distance, becoming comparable with the cylinder radius a at distances of $O(\mathrm{Re}\ a)$. Prior to this, the layer is thin compared to the radius and the flow is close to the Blasius profile of a flat plate. However, it differs from the Blasius solution due to effects of curvature and rotation at larger downstream distances. As S increases, the centrifugal force creates an increasing radial pressure gradient, which combined with axial development, implies an increasing axial gradient of pressure. Above $S = 4.15$, the maximum velocity exceeds the free-stream velocity for a range of Z and we say that a wall jet exists. This jet becomes stronger and stronger as $S \to \infty$.

In the limit of large Z, we find that the axial and radial components of velocity decouple from the azimuthal velocity component and pressure. All these quantities are found to have asymptotic expansions in inverse powers of $\ln(Z)$, a result already obtained for the non-rotating case by Glauert & Lighthill [3], and here extended to include rotation. The leading-order term in the u_θ expansion is $u_\theta \sim SR^{-1}$, which is the flow expected for a rotating cylinder, infinite in both directions. Because U_θ becomes independent of Z, the same is true of the pressure field resulting from the centrifugal force, hence the absence of an axial pressure gradient to drive the axial/radial flow. This is the reason for the decoupling.

When S is large, we introduce appropriate scalings for Z, U_z, U_θ and P. The asymptotic expansions of the scaled velocity and pressure proceed as inverse powers of S, beginning with S^0. The leading-order term describes an axial wall jet due to a rotating cylinder in a fluid at rest.

Funding statement. The authors are grateful to the French Ministry of Education and Research and the Indo-French Centre for the Promotion of Advanced Research-CEFIPRA for financial support.

A. Large Z asymptotic expansions

The flow variables are expressed as asymptotic expansions in inverse powers of χ:

$$U_z \sim 1 + \sum_{n=1}^{\infty} \chi^{-n} U_z^{(n)}(\eta), \tag{A.1}$$

$$U_r \sim \sum_{n=1}^{\infty} \chi^{-n} U_r^{(n)}(\eta), \tag{A.2}$$

$$U_\theta \sim S \sum_{n=1}^{\infty} \chi^{-n+1} U_\theta^{(n)}(\eta), \tag{A.3}$$

$$P \sim S^2 \sum_{n=1}^{\infty} \chi^{-n+1} P^{(n)}(\eta). \tag{A.4}$$

Introducing these expansions into equations (5.2)–(5.5) gives

$$\frac{1}{\eta}\frac{\mathrm{d}}{\mathrm{d}\eta}\left(\eta \frac{\mathrm{d}U_z^{(n)}}{\mathrm{d}\eta}\right) + \eta \frac{\mathrm{d}U_z^{(n)}}{\mathrm{d}\eta} = \phi_z^{(n)}, \tag{A.5}$$

$$\eta^3 \frac{\mathrm{d}}{\mathrm{d}\eta}\left(\frac{P^{(n)}}{\eta^2}\right) = \psi^{(n)}, \tag{A.6}$$

$$\eta \frac{\mathrm{d}}{\mathrm{d}\eta}\left(\frac{1}{\eta}\frac{\mathrm{d}U_\theta^{(n)}}{\mathrm{d}\eta}\right) + \eta \frac{\mathrm{d}U_\theta^{(n)}}{\mathrm{d}\eta} = \phi_\theta^{(n)}, \tag{A.7}$$

$$\frac{1}{\eta}\frac{\mathrm{d}U_r^{(n)}}{\mathrm{d}\eta} - \eta \frac{\mathrm{d}U_z^{(n)}}{\mathrm{d}\eta} = \phi_r^{(n)}, \tag{A.8}$$

where

$$\phi_z^{(n)} = (1-n)U_z^{(n-1)} + \sum_m \left(\left(\frac{U_r^{(m)}}{\eta} - \eta U_z^{(m)}\right)\frac{\mathrm{d}U_z^{(n-m)}}{\mathrm{d}\eta} - m U_z^{(m)} U_z^{(n-m-1)}\right), \tag{A.9}$$

$$\phi_\theta^{(n)} = (2-n)U_\theta^{(n-1)} + \sum_m \left(\left(\frac{U_r^{(m)}}{\eta} - \eta U_z^{(m)}\right)\frac{\mathrm{d}U_\theta^{(n-m)}}{\mathrm{d}\eta} - (m-1) U_\theta^{(m)} U_z^{(n-m-1)}\right), \tag{A.10}$$

$$\phi_r^{(n)} = (n-1)U_z^{(n-1)}, \qquad \psi^{(n)} = \sum_m U_\theta^{(m)} U_\theta^{(n-m+1)}. \tag{A.11}$$

Equations (A.5)–(A.8) are to be solved, along with appropriate boundary conditions (which will be derived shortly), for the nth-order coefficients of the expansions, $U_z^{(n)}, U_r^{(n)}, U_\theta^{(n)}$ and $P^{(n)}$ ($n \geq 1$). It should be noted that, in equations (A.9)–(A.11), $U_z^{(m)}$, $U_r^{(m)}$ and $U_\theta^{(m)}$ are to be interpreted as zero when $m \leq 0$. The governing equations for $U_z^{(n)}$ and $U_r^{(n)}$ are independent of $U_\theta^{(n)}$ and $P^{(n)}$. Thus, the asymptotics of $U_z^{(n)}$ and $U_r^{(n)}$ are the same as for a non-rotating cylinder and are governed by equations (A.5), (A.8), (A.9) and the first of the equations (A.11). $U_\theta^{(n)}$ is determined by equations (A.7) and (A.10), while $P^{(n)}$ follows from equation (A.6) and the second of the equations (A.11). Note that $\phi_z^{(n)}$, $\phi_r^{(n)}$ and $\phi_\theta^{(n)}$ depend only on the solution at lower orders than n, suggesting a method which proceeds from $n = 1$ to successively higher values of n.

The boundary conditions at $\eta \to \infty$ are

$$U_z^{(n)} = U_\theta^{(n)} = P^{(n)} = 0. \tag{A.12}$$

Application of the boundary conditions (2.15) at the cylinder surface requires the introduction of an inner region, $R = O(1)$, represented by the expansions

$$U_z \sim \sum_{n=1}^{\infty} \chi^{-n} \hat{U}_z^{(n)}(R), \tag{A.13}$$

$$U_r \sim \sum_{n=1}^{\infty} \chi^{-n} \hat{U}_r^{(n)}(R), \tag{A.14}$$

$$U_\theta \sim S \sum_{n=1}^{\infty} \chi^{-n+1} \hat{U}_\theta^{(n)}(R), \tag{A.15}$$

$$P \sim S^2 \sum_{n=1}^{\infty} \chi^{-n+1} \hat{P}^{(n)}(R). \tag{A.16}$$

Equations (2.11), (2.13) and (2.14) are rewritten using the axial coordinate χ in place of Z. Equation (2.14) yields

$$\frac{\partial \hat{U}_r^{(n)}}{\partial R} = 0, \tag{A.17}$$

which, together with the boundary conditions (2.15) gives $\hat{U}_r^{(n)} = 0$. Equations (2.11) and (2.13) imply

$$\frac{\partial^2 \hat{U}_z^{(n)}}{\partial R^2} + \frac{1}{R} \frac{\partial \hat{U}_z^{(n)}}{\partial R} = 0, \tag{A.18}$$

$$\frac{\partial^2 \hat{U}_\theta^{(n)}}{\partial R^2} - \frac{1}{R} \frac{\partial \hat{U}_\theta^{(n)}}{\partial R} = 0, \tag{A.19}$$

hence

$$\hat{U}_z^{(n)}(R) = A_n \ln R + B_n, \tag{A.20}$$

$$\hat{U}_\theta^{(n)}(R) = C_n R^2 + D_n. \tag{A.21}$$

The boundary conditions (2.15) imply $B_n = 0$, $C_1 + D_1 = 1$, and $C_n + D_n = 0$ for $n > 1$.

Recalling that $R = \zeta\eta = e^{\chi}\eta$, the inner expansions give

$$U_z \sim A_1 + \sum_{n=1}^{\infty} \chi^{-n}(A_n \ln \eta + A_{n+1}), \tag{A.22}$$

$$U_\theta \sim S\left(1 + \sum_{n=1}^{\infty} C_n \chi^{-n}(e^{2\chi}\eta^2 - 1)\right), \tag{A.23}$$

$$U_r \sim 0, \tag{A.24}$$

when expressed in terms of the outer coordinate, η. Matching requires $A_1 = 1$, $C_n = 0$ and

$$U_z^{(n)} \sim A_n \ln \eta + A_{n+1}, \tag{A.25}$$

$$U_\theta^{(1)} \to 1 \quad \text{and} \quad U_\theta^{(n)} \to 0 \quad \text{for} \quad n > 1, \tag{A.26}$$

$$U_r^{(n)} \to 0, \tag{A.27}$$

as $\eta \to 0$. It follows from (A.25) that

$$\eta \frac{\mathrm{d}U_z^{(n)}}{\mathrm{d}\eta} \to A_n \tag{A.28}$$

and

$$A_{n+1} = \lim_{\eta \to 0} \left(U_z^{(n)} - A_n \ln \eta \right). \tag{A.29}$$

Assuming A_n is known, equations (A.5)–(A.11) and the boundary conditions (A.12) and (A.26)–(A.28) can be solved for $U_z^{(n)}$, $U_r^{(n)}$, $U_\theta^{(n)}$ and $P^{(n)}$. $A_1 = 1$ gets the process started and leads to the leading-order outer solution, (5.8)–(5.11), in agreement with [3]. Equation (A.29) gives A_n at the next order, allowing solution at successively higher orders. It can be shown that

$$U_z^{(n)} = A_n \ln \eta + A_{n+1} + O(\eta^2 \ln^{p_n} \eta), \quad U_\theta^{(n)} = 1 - q_n + O(\eta^2), \quad U_r^{(n)} = O(\eta^2 \ln^{q_n} \eta), \tag{A.30}$$

as $\eta \to 0$, where $q_n = p_{n+1} - 1, p_1 = 0, p_2 = 1$ and $p_n = 2$ for $n \geq 3$. The terms in (A.30) indicated by the $O()$ notation are exponentially small in the inner region, while the remaining ones reproduce the inner solution. Thus, the outer expansions in fact apply in the inner region.

The above procedure has been implemented numerically and results up to $n = 5$ are presented in figure 12. Figure 13 shows the comparison of numerical solution of U_z at $Z = 5000$ and $S = 1$ with the asymptotic solution obtained by truncating at different orders n. Although this result shows good convergence, and therefore further confirms both numerical and analytical results, it should be borne in mind that the expansions (A.1)–(A.4) are, in fact, asymptotic as $Z \to \infty$, rather than necessarily convergent at any finite Z.

B. Flow over the nose

Large Reynolds number implies a thin boundary layer over the nose. Schlichting [11] gives the axisymmetric boundary-layer equations in terms of curvilinear coordinates, x, y, θ, where x is distance along the surface, and y is distance normal to the surface. Here we use the non-dimensional coordinates, velocity components and pressure:

$$\tilde{y} = \mathrm{Re}^{\frac{1}{2}} y/a, \quad \tilde{x} = x/a, \tag{B.1}$$

$$\tilde{u}_y = \mathrm{Re}^{\frac{1}{2}} u_y / U_\infty, \quad \tilde{u}_x = u_x/U_\infty, \quad \tilde{u}_\theta = u_\theta/U_\infty, \quad \tilde{p} = p. \tag{B.2}$$

The boundary-layer equations in these variables are

$$\tilde{u}_x \frac{\partial \tilde{u}_x}{\partial \tilde{x}} + \tilde{u}_y \frac{\partial \tilde{u}_x}{\partial \tilde{y}} - \frac{\tilde{u}_\theta^2}{\tilde{R}} \frac{\mathrm{d}\tilde{R}}{\mathrm{d}\tilde{x}} = -\frac{\partial \tilde{p}}{\partial \tilde{x}} + \frac{\partial^2 \tilde{u}_x}{\partial \tilde{y}^2}, \tag{B.3}$$

$$\tilde{u}_x \frac{\partial \tilde{u}_\theta}{\partial \tilde{x}} + \tilde{u}_y \frac{\partial \tilde{u}_\theta}{\partial \tilde{y}} + \frac{\tilde{u}_\theta \tilde{u}_x}{\tilde{R}} \frac{\mathrm{d}\tilde{R}}{\mathrm{d}\tilde{x}} = \frac{\partial^2 \tilde{u}_\theta}{\partial \tilde{y}^2}, \tag{B.4}$$

$$\frac{\partial \tilde{p}}{\partial \tilde{y}} = 0,$$

$$\frac{\partial \tilde{u}_x}{\partial \tilde{x}} + \frac{\tilde{u}_x}{\tilde{R}} \frac{d\tilde{R}}{d\tilde{x}} + \frac{\partial \tilde{u}_y}{\partial \tilde{y}} = 0, \tag{B.5}$$

with the boundary conditions

$$\tilde{u}_x = \tilde{u}_y = 0, \tilde{u}_\theta = S\tilde{R}(\tilde{x}) \quad \tilde{y} = 0, \tag{B.6}$$

$$\tilde{u}_x \to U_{ext}(\tilde{x}), \tilde{u}_\theta \to 0 \quad \tilde{y} \to \infty, \tag{B.7}$$

where the nose geometry is represented by $r = \tilde{R}(\tilde{x})$ and $U_{ext}(\tilde{x})$ is the velocity just outside the boundary layer. Equations (B.3)–(B.5) can, in principle, be solved to obtain the flow over the nose. Note the centrifugal term in equation (B.3), which will no doubt produce a wall jet on the nose at sufficiently large S. The terms containing $\mathrm{d}\tilde{R}/\mathrm{d}\tilde{x}$ vanish on the constant-radius cylinder (where $\tilde{x}$

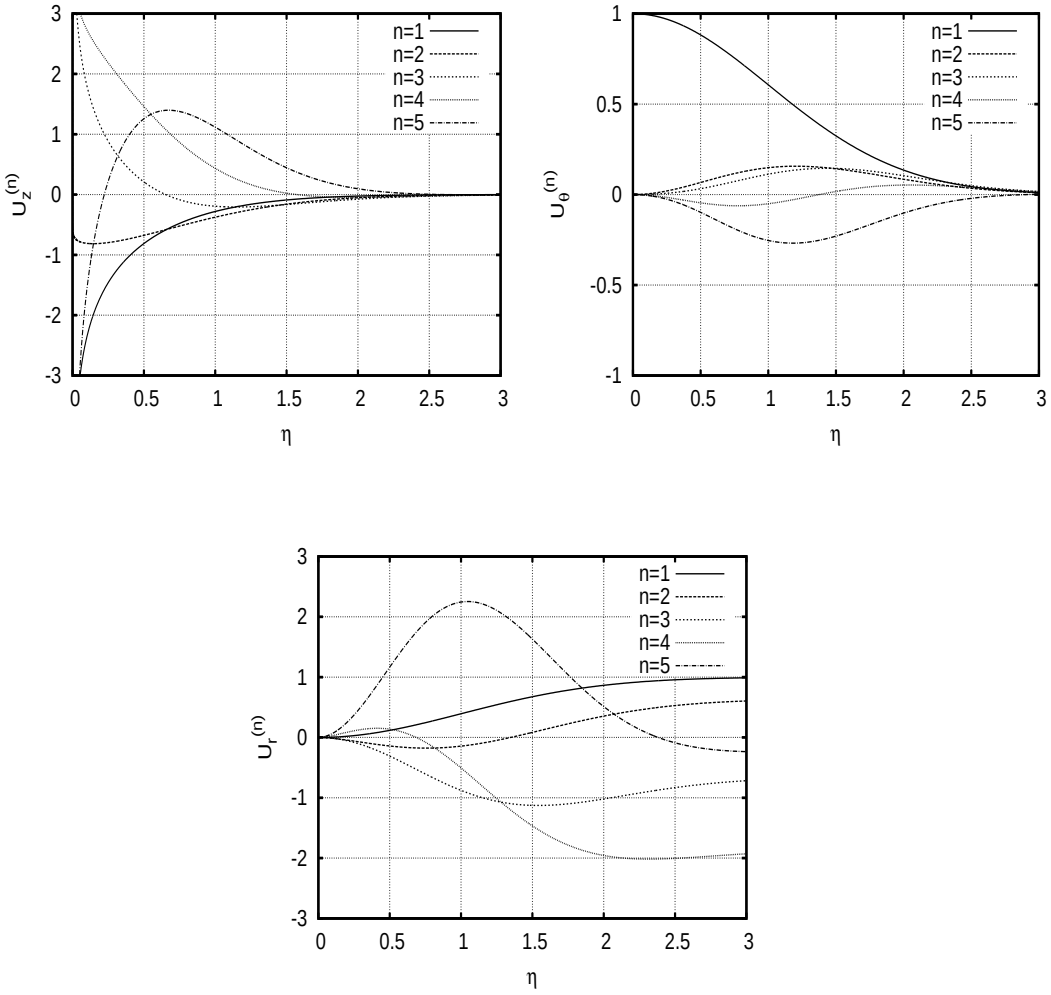

Figure 12. First five coefficients of the large-Z asymptotic expansions of U_z, U_θ and U_r.

and z coincide to within an additive constant) and equations (B.3)–(B.5) then become those of a flat-plate. Thus, we expect the flow to approach the Blasius solution as $\tilde{x} \to \infty$. There are, in fact, two asymptotic regions, $\tilde{x} = O(1)$ and $\tilde{x} = O(\mathrm{Re})$, the former being described by equations (B.3)–(B.5) and the latter by equations (2.11)–(2.14). Matching of the regions requires the Blasius flow as inlet conditions to the latter equations, as noted in the main text. Thus, the flow in the region $Z = O(1)$, which is the subject of this paper, is insensitive to the geometry of the nose. Note that a wall jet may appear on the nose, subsequently disappearing on the cylinder, later reappearing in the region $Z = O(1)$.

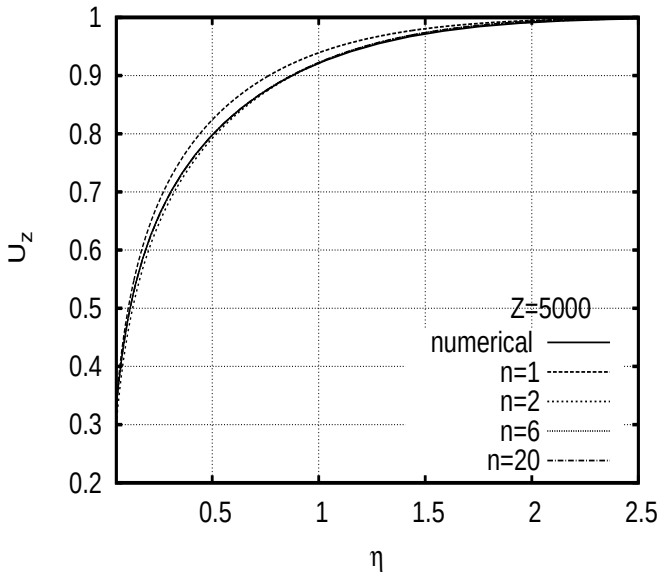

Figure 13. Comparison of the numerical solution of U_z with the large-Z asymptotic solution truncated at different orders for $Z = 5000$ at $S = 1$.

References

1. Seban RA and Bond R. 1951 Skin-friction and heat-transfer characteristics of a laminar boundary layer on a cylinder in axial incompressible flow. *Journal of the Aeronautical Sciences*. **18**, 10 (doi:10.2514/8.2076).
2. Kelly HR. 1954 A note on the laminar boundary layer on a circular cylinder in axial incompressible flow. *Journal of the Aeronautical Sciences (Institute of the Aeronautical Sciences)*. **21**, 9 (doi:10.2514/8.3151).
3. Glauert MB and Lighthill MJ. 1955 The axisymmetric boundary layer on a long thin cylinder. *Proc. R. Soc. A*. **230**, 1181, 188-203 (doi:10.1098/rspa.1955.0121).
4. Jaffe NA and Okamura TT. 1968 The transverse curvature effect on the incompressible laminar boundary layer for longitudinal flow over a cylinder. *Zeitschrift für angewandte Mathematik und Physik ZAMP*. **19**, 4, 564-574 (doi:10.1007/BF01594964).
5. Tutty OR and Price WG and Parsons AT. 2002 Boundary layer flow on a long thin cylinder. *Physics of Fluids*. **14**, 628 (doi:10.1063/1.1427921).
6. Vinod N and Govindarajan R. 1955 Secondary instabilities in incompressible axisymmetric boundary layers: Effect of transverse curvature. *Journal of Fluids Engineering, Transactions of the ASME*. **134**, 2 (doi:10.1115/1.4005767).
7. Petrov GV. 1976 Boundary layer on a rotating cylinder in axial flow. *Journal of Applied Mechanics and Technical Physics*. **17**, 4, 506-510 (doi:10.1007/BF00852000).
8. Kao KH and Chow CY. 1991 Stability of the boundary layer on a spinning semi-infinite circular cylinder. *Journal of Spacecraft and Rockets*. **28**, 3, 284-291 (doi:10.2514/3.26242).
9. Herrada MA and Del Pino C and Fernandez-Feria R. 2008 Stability of the boundary layer flow on a long thin rotating cylinder. *Physics of Fluids*. **20**, 3 (doi:10.1063/1.2885330).
10. Batchelor GK. 1967 *An Introduction to Fluid Dynamics*, Cambridge University Press
11. Schlichting H. 1956 Laminar flow about a rotating body of revolution in an axial airstream. *Ingenieur-Archives*. **21**, 4, 227-244 (http://ntrs.nasa.gov/archive/nasa/20050019631.pdf).
12. Scott JF. 2013 Moffatt-type flows in a trihedral cone. *Journal of Fluid Mechanics*. **725**, 446-461 (doi:10.1017/jfm.2013.180).